Transactions in Optics and Photonics
https://ojs.wiserpub.com/index.php/TOP/

Research Article

Role of Tunable Nonlinearities of Metamaterials on Tightly Focused Beam Generation

N. K. Hashim[1,4], Mustafa Bayram[2], A. K. Shafeeque Ali[3*], Gopi Somasundaram[4†]

[1] Department of Physics, W. M. O. Arts and Science College, Muttil, Kerala, India
[2] Department of Computer Engineering, Biruni University, Istanbul, Turkey
[3] Department of Physics, Sullamussalam Science College, Areekode, Kerala, India
[4] Department of Physics, Sri Ramakrishna Mission Vidyalaya College of Arts and Science, Coimbatore, Tamil Nadu, India
E-mail: shafeequeali3@sscollege.ac.in, ssgopi1992@gmail.com

Received: 2 March 2025; **Revised:** 16 April 2025; **Accepted:** 14 May 2025

Abstract: MetaMaterials (MMs) offer strong tunability of optical properties, enabling diverse photonic applications. We investigate the role of tunable optical nonlinearities in the formation of Tightly Focused Beam (TFB). The system is described by a nonlinear Schrödinger equation, and modulation instability is analyzed both analytically and numerically to identify parameter regimes supporting localized beam formation. The dynamics of Gaussian and hollow Gaussian beams are further studied using numerical simulations, with emphasis on TFB generation. Results show that adjustable nonlinearities in MMs significantly enhance control over beam focusing characteristics. Notably, hollow Gaussian beams generate higher-intensity TFB clusters compared to standard Gaussian beams. These findings suggest potential applications in optical trapping and high-density data storage.

***Keywords*:** modulation instability, metamaterials, extreme events

Abbreviation

MMs	MetaMaterials
TFB	Tightly Focused Beam
HGB	Hollow Gaussian Beam
MI	Modulation Instability
FWHM	Full Width at Half Maximum

1. Introduction

The tightly focused optical beams, which are laser beams concentrated into tiny spots, exhibit complex and flexible electric field distributions. The Tightly Focused Beams (TFBs) have been found to have applications in optical tweezers, which are used to trap and manipulate tiny objects, such as biological cells and molecules [1, 2]. A metasurface has been proposed to realize the structured light fields and to generate a superposition of profile-tunable tightly focused vector beams [3]. A method has been developed to generate TFB with adjustable spin orientation [4]. Recently, the auto-focusing

DOI:

characteristics of a symmetric butterfly Gaussian beam have been reported [5]. Moreover, the experimental observation of three-dimensional optical trapping by a tightly focused circular Airy beam has been reported [6].

It is well known that one of the challenges in realizing structured light beams and TFBs is the immutability of material parameters associated with natural materials. MetaMaterials (MMs) are one of the choices that provide engineering freedom to tune material parameters. The MMs are found to exhibit many exotic behaviors that are not attainable in natural materials. Their unique sub-wavelength structuring enables exotic responses such as negative refractive index, optical magnetism, and tailored anisotropy, which have led to breakthroughs in super-resolution imaging, cloaking, dispersion engineering, and ultra-fast nanophotonics [7]. Recent research has demonstrated hyperbolic dispersion in three-dimensional MMs [8], asymmetric transmission using chiral optical MMs [9], and polarization manipulation at optical frequencies [10]. The quantum-enabled MMs and nonlinear metasurfaces have opened avenues for controlling spontaneous emission, generating high-harmonic signals, and manipulating entangled photon states [11–13].

In this research, we adopt the tunability of nonlinearities in the MMs to generate the TFBs with adjustable attributes. The nonlinear MMs exploit engineered sub-wavelength structures to enhance or tailor nonlinear optical responses, enabling functionalities such as frequency conversion, ultra-fast all-optical switching, and high-harmonic generation that are far stronger than those in natural materials [14, 15]. Also, research has demonstrated metasurfaces with giant second- and third-order susceptibilities ($\chi^{(2)}$ and $\chi^{(3)}$), enabling compact platforms for nonlinear wavefront control, quantum light generation, and tunable nonlinear photonic devices [16]. Taking advantage of the tunability of the nonlinear parameters of MMs, we study Modulation Instability (MI) to explore the parametric region of the material to form a localized optical beam. The process of MI plays a central role in the formation of optical solitons, supercontinuum generation, and frequency comb development [17–20]. MI also underpins complex dynamical behaviors such as chaotic pulse evolution and rogue-wave emergence in both optical and hydrodynamic systems. Furthermore, researchers have explored higher-order MI in nonlinear optics, resulting from the nonlinear superposition of elementary instabilities [21].

2. Modulation instability

A generalized system of coupled nonlinear Schrödinger equations describing a few-cycle pulse propagation in a MM with both nonlinear electric polarization and nonlinear magnetization has been derived [22]. Based on a 3 + 1 dimensional nonlinear Schrödinger equation describing ultrashort electromagnetic pulse propagation in metamaterial, the existence of a spatiotemporal electromagnetic soliton has been predicted [23]. Following the same mathematical model, the stabilization and interaction dynamics of spatiotemporal solitons in MMs have been reported [24]. The behavior of extremely powerful electromagnetic waves as they travel through MMs exhibiting cubic and quintic nonlinear properties can be accurately modeled using a specific nonlinear mathematical framework, namely the nonlinear Schrödinger equation [25–27],

$$\frac{\partial V}{\partial z} - i\frac{\mathrm{sgn}(n)}{2}\left(\frac{\partial^2 V}{\partial x^2} + \frac{\partial^2 V}{\partial y^2}\right) - i\rho_1|V|^2V - i\rho_2|V|^4V = 0, \tag{1}$$

where $V(x, y, z)$ represents the slowly varying, normalized complex envelope of the beam. The coordinates x and y denote the transverse directions, while z signifies the distance of propagation. The term $\mathrm{sgn}(n)$ indicates the sign of the refractive index, with $+1$ and -1 corresponding to positive and negative indices, respectively. The coefficients ρ_1 and ρ_2 represent the normalized cubic and quintic nonlinearities, respectively. In the present work, we have employed a lossless cubic-quintic nonlinear Schrödinger equation to isolate and analyze the fundamental role of tunable nonlinearities on MI and beam localization. This approximation is justified in the context of loss-compensated or active metamaterials, which have been extensively demonstrated in the literature. Recent advances have shown that the intrinsic losses in metamaterials can be effectively mitigated or even compensated by incorporating active components such as optical gain media, electrically pumped gain layers, and rare-earth-doped dielectric hosts [28, 29]. In such systems, the effective linear loss coefficient can be significantly reduced or brought close to zero, resulting in near-lossless or even amplifying regimes.

To examine MI in the metamaterial, we conduct a linear stability analysis based on the mathematical model described by Eq. (1). This involves perturbing the continuous wave solution of the model and analyzing the evolution of the perturbation with propagation distance. The growth or decay of the perturbation can generate the ultra-short pulses. Now we assume the steady-state solution of Eq. (1) is:

$$V = \sqrt{P}\, e^{(i\varphi z)}, \tag{2}$$

where P stands for the input power. $\varphi = \rho_1 P + \rho_2 P^2$ is the nonlinear phase shift. To analyze the stability of Eq. (2), perturb the solution by inserting a small disturbance $\varsigma(x,\ y,\ z)$ to the amplitude such that,

$$V = (\sqrt{P} + \varsigma(x,\ y,\ z))\, e^{(i\varphi z)}. \tag{3}$$

Now we insert Eq. (3) into Eq. (1) and following standard procedure of linear stability analysis [30–32], one can obtain the stability matrix as follows,

$$G = \begin{pmatrix} \chi_{11} & \chi_{12} \\ \chi_{21} & \chi_{22} \end{pmatrix}$$

here $\chi_{11} = 0$, $\chi_{12} = \frac{1}{2}\mathrm{sgn}(n)(L_x^2 + L_y^2)$, $\chi_{21} = 2\rho_1 P + 4\rho_2 P^2 - \frac{1}{2}\mathrm{sgn}(n)((L_x^2 + L_y^2))$ and $\chi_{22} = 0$. The gain spectrum of MI is characterized by the positive real part of the eigenvalue obtained from the stability matrix, which provides a measure of the growth rate of the instability. where L_x and L_y stand for the transverse wave numbers.

$$\mathrm{Gain} = \mathrm{Re}(\psi), \tag{4}$$

where ψ is the eigenvalue of the matrix G and Re represents the real part.

Figure 1 depicts the spatial instability in MMs as a function of input optical power. Figure 1(a) and (d) represent the MI in the presence of cubic nonlinearity alone ($|\rho_1| = 1$ and $|\rho_2| = 0$). A closer examination of the MI reveals that the input optical power has a threshold value, below which the instability is absent. This threshold power is a critical parameter that determines the onset of nonlinear effects. In the presence of cubic nonlinearity alone, the eigenvalue of the matrix G is given by

$$\psi = \pm\frac{1}{2}\{-\mathrm{sgn}(n)L^2[-4\rho_1 P + \mathrm{sgn}(n)L^2]\}^{1/2}, \tag{5}$$

where $L^2 = L_x^2 + L_y^2$. The onset of MI is obtained by setting the radicand equal to zero:

$$-4\rho_1 P + \mathrm{sgn}(n)L^2 = 0. \tag{6}$$

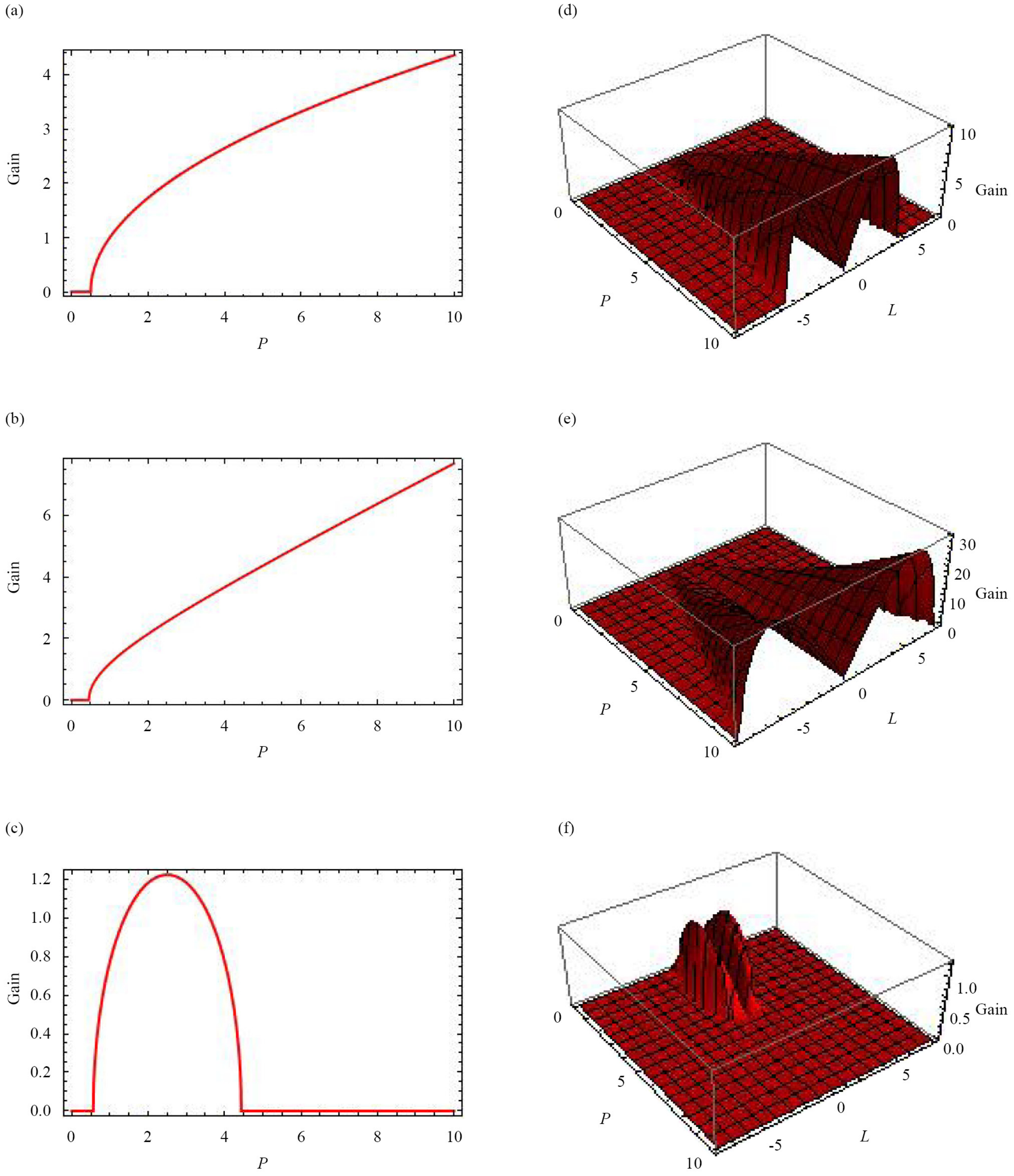

Figure 1. Spatial MI in MMs as a function of optical power. (a, d) MI observed in a cubic nonlinear MM. (b, e) MI observed in a cooperating cubic and quintic nonlinear MM. (c, f) MI observed in a competing cubic and quintic nonlinear MM. Where $L = L_x = L_y$

Solving for the threshold power, we obtain

$$P_{T1}=\frac{\mathrm{sgn}(n)L^2}{4\rho_1}. \tag{7}$$

Thus, MI occurs only when $P > P_{T1}$. For the case of combined cubic and quintic nonlinearities, the eigenvalue is

$$\psi=\pm\frac{1}{2}\{-\mathrm{sgn}(n)L^2[-4\rho_1 P-8\rho_2 P^2+\mathrm{sgn}(n)L^2]\}^{1/2}. \tag{8}$$

Setting the radicand to zero gives the threshold condition:

$$-4\rho_1 P-8\rho_2 P^2+\mathrm{sgn}(n)L^2=0. \tag{9}$$

This is a quadratic equation in P, which yields

$$P_{T2}=\frac{-\rho_1+\sqrt{\rho_1^2+2\rho_2\mathrm{sgn}(n)L^2}}{4\rho_2}, \tag{10}$$

where the physically relevant root corresponds to the positive value of P. The analytical expressions for the threshold powers P_{T1} and P_{T2} are in good agreement with the numerical MI spectra presented in Figure 1. For the purely cubic case, the analytical threshold predicts that MI occurs only when $P > P_{T1}$. This behavior is clearly observed in Figure 1(a, d), where the MI gain is absent below a certain input power and emerges only after exceeding the threshold. Furthermore, the dependence of P_{T1} on the transverse wavenumber L is consistent with the numerical gain spectrum, where higher values of L require larger input power to trigger instability. For the cubic–quintic case, the analytical threshold accurately captures the shift in the onset of MI observed in Figure 1(b, e). In the case of cooperating nonlinearities ($\rho_1\rho_2 > 0$), the threshold is reduced compared to the purely cubic case, leading to an earlier onset and enhanced gain region. This trend is consistent with the broader and stronger MI bands seen in the numerical results. In contrast, for competing nonlinearities ($\rho_1\rho_2 < 0$), the analytical expression predicts an increase in the effective threshold and a restricted instability region. This is in agreement with Figure 1(c, f), where the MI gain initially appears but is subsequently suppressed at higher powers, indicating a limited range of instability. The competing nonlinearities can ultimately suppress MI by attenuating perturbative modes [33]. In the subsequent section, we conduct numerical experiments to investigate the evolution of perturbed continuous waves, to validate our analytical results, and explore the generation of localized modes as a consequence of spatial instability.

We initiate our simulations with a perturbed continuous wave, which serves as the initial condition. This perturbed continuous wave is mathematically represented in the following form:

$$V(0,x,y)=\sqrt{P}+\Lambda[cos(\eta x)+cos(\eta y)]. \tag{11}$$

The perturbed continuous wave is characterized by two key parameters: the perturbation amplitude, denoted by Λ, and the wave number, represented by η. These parameters play a crucial role in determining the evolution of the perturbed continuous wave. To investigate this evolution, we numerically solve Eq. (1) with the initial condition given in Eq. (11) using the Mathematica software package. For our numerical simulation, we define the computational domain as $x\in[-4,\ 4]$ and $y\in[-4,\ 4]$. We impose the function to vanish at the boundaries ($V(z,\ -4,\ y)=V(z,\ 4,\ y)=0$ and

$V(z,x,-4) = V(z,x,4) = 0$ for x and y, respectively). We also set the simulation parameters as $\Lambda = 0.001$ and $\eta = 4$. Also, here we use the normalized nonlinear coefficients ρ_1 and ρ_2 ($|\rho_1| = 1$ and $|\rho_2| = 0.1$), which can be related to dimensional material parameters by introducing characteristic scales for the transverse length w_0 and the diffraction length $z_0 = k_0 w_0^2$, where $k_0 = 2\pi n_0/\lambda$ is the carrier wavenumber. Writing the dimensional field as $A(x,\, y,\, z)$, the governing equation takes the form

$$i\frac{\partial A}{\partial z} + \frac{1}{2k_0}\nabla_\perp^2 A + k_0 n_2 |A|^2 A + k_0 n_4 |A|^4 A = 0, \tag{12}$$

where n_2 and n_4 are the cubic and quintic nonlinear refractive indices, respectively.

Using the normalization

$$x = \frac{x'}{w_0}, \quad y = \frac{y'}{w_0}, \quad z = \frac{z'}{z_0}, \quad V = \frac{A}{A_0}, \tag{13}$$

we obtain the dimensionless equation (Eq. (1)) with

$$\rho_1 = k_0 n_2 A_0^2 z_0, \quad \rho_2 = k_0 n_4 A_0^4 z_0. \tag{14}$$

Thus, the chosen normalized values $\rho_1 = \pm 1$ and $\rho_2 = \pm 0.1$ correspond to the conditions

$$k_0 n_2 A_0^2 z_0 \sim 1, \quad k_0 n_4 A_0^4 z_0 \sim 0.1. \tag{15}$$

For experimentally relevant metamaterials and metasurfaces operating at near-infrared wavelengths ($\lambda \sim 1.55\ \mu$m), typical parameters are:

- Refractive index: $n_0 \sim 1$–3;
- Cubic nonlinearity: $n_2 \sim 10^{-16}$–10^{-14} m^2/W (enhanced up to 10^{-13} m^2/W in resonant or Epsilon Near Zero (ENZ) metamaterials);
- Quintic nonlinearity: $n_4 \sim 10^{-30}$–10^{-26} m^4/W^2;
- Beam waist: $w_0 \sim 1$–$5\ \mu$m;
- Peak intensity: $I \sim 10^{10}$–10^{12} W/m^2.

Using $A_0^2 \propto I$ and $z_0 = k_0 w_0^2$, these values yield

$$\rho_1 \sim \mathcal{O}(1), \quad \rho_2 \sim 0.01\text{–}0.1, \tag{16}$$

which are consistent with the normalized parameters used in this work.

We begin by examining the case of an MM that exhibits cubic nonlinearity alone ($|\rho_1| = 1$). To ensure that MI-induced processes are prominent, we consider an optical power above the threshold value. Figure 2 presents the results of numerical simulations on spatial MI of a continuous wave in MMs with cubic nonlinearity. The input perturbed continuous wave with a power of P = 1 is illustrated in Figure 2a. As the perturbed continuous wave propagates through the MM with cubic nonlinearity, the interplay between nonlinearity and diffraction causes the perturbation to grow, as shown in Figure 2b. Upon further propagation, the perturbation still grows due to MI, and the localized wave continues to absorb energy from the surrounding wavepackets, leading to a substantial increase in its intensity to form a TFB.

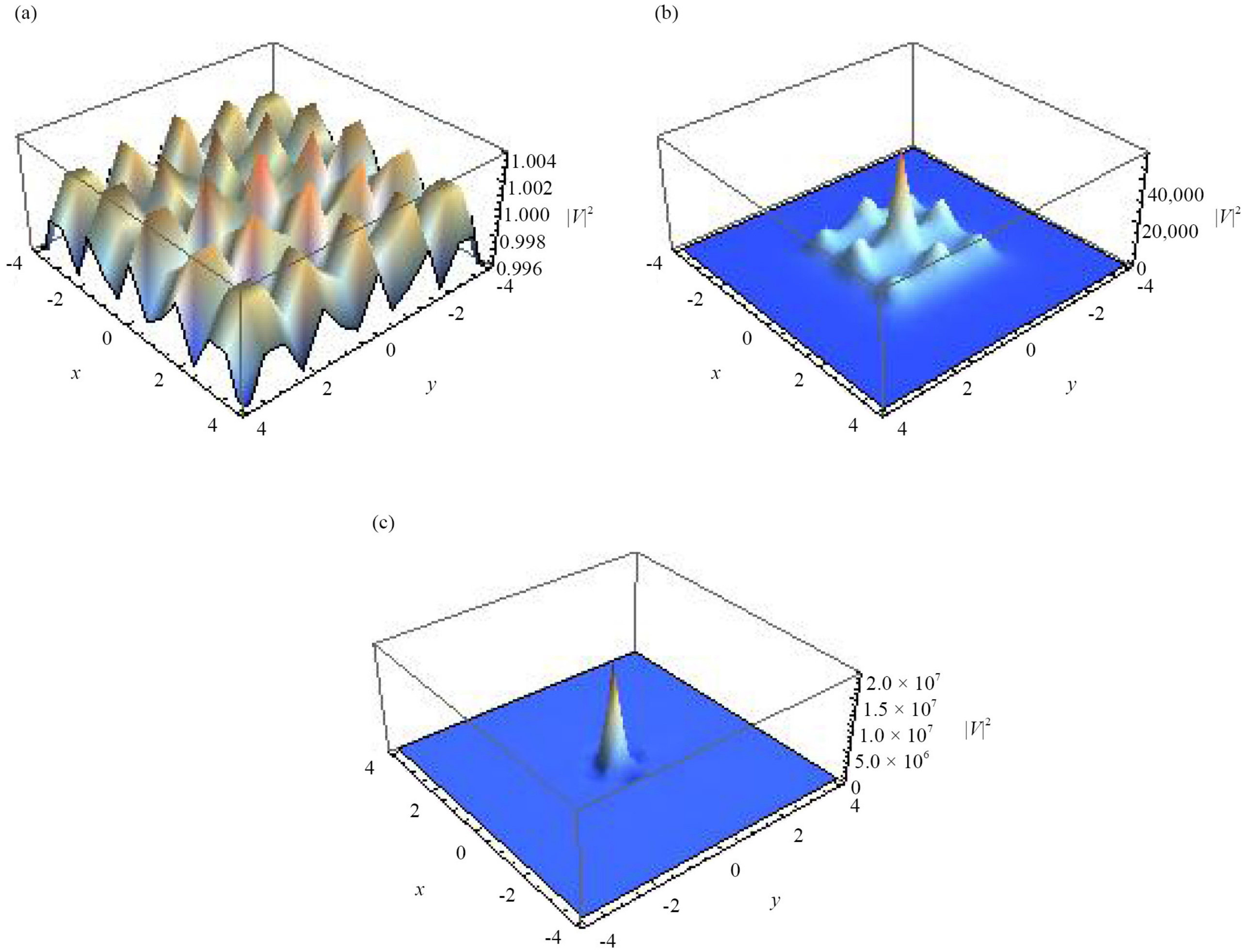

Figure 2. Numerical simulation on spatial MI of continuous wave in MMs with cubic nonlinearity ($|\rho_1| = 1$ and $|\rho_2| = 0$) when optical power $P = 1$. (a) Input perturbed continuous wave. (b) and (c) represent evolution stages showing the exponential growth of perturbation imposed on the continuous wave to form a TFB. Other parameters are $\Lambda = 0.001$ and $\eta = 4$

We now turn our attention to the nature of MI-induced TFB in MMs that exhibit both cubic and quintic nonlinearities, which cooperate. Our linear stability analysis and Figure 1(b) reveal that the presence of these cooperating nonlinearities enhances the MI gain, leading to a more unstable environment. This enhancement in MI gain has a direct impact on the characteristics of the TFB that emerge, increasing their peak amplitude. Figure 3(a)-(c) illustrate the formation of TFB as a result of spatial instability in MMs with cooperating cubic and quintic nonlinearities when a perturbed continuous wave (refer to Figure 2a) with a power of $P = 1$ evolves in the medium. A clear trend emerges from this figure, demonstrating that the cooperation between cubic and quintic nonlinearities leads to an increase in the amplitude, and it leads to tighter focusing. This behavior is consistent with our expectations, as the interplay between these nonlinearities amplifies the instability gain, giving rise to more intense localized structure. Furthermore, Figure 3(d) shows that the competition between cubic and quintic nonlinearities suppresses the instability gain, giving rise to a less intense localized structure. The engineering flexibility of MMs allows for precise control over material parameters, enabling tunable MI and TFB with customizable properties.

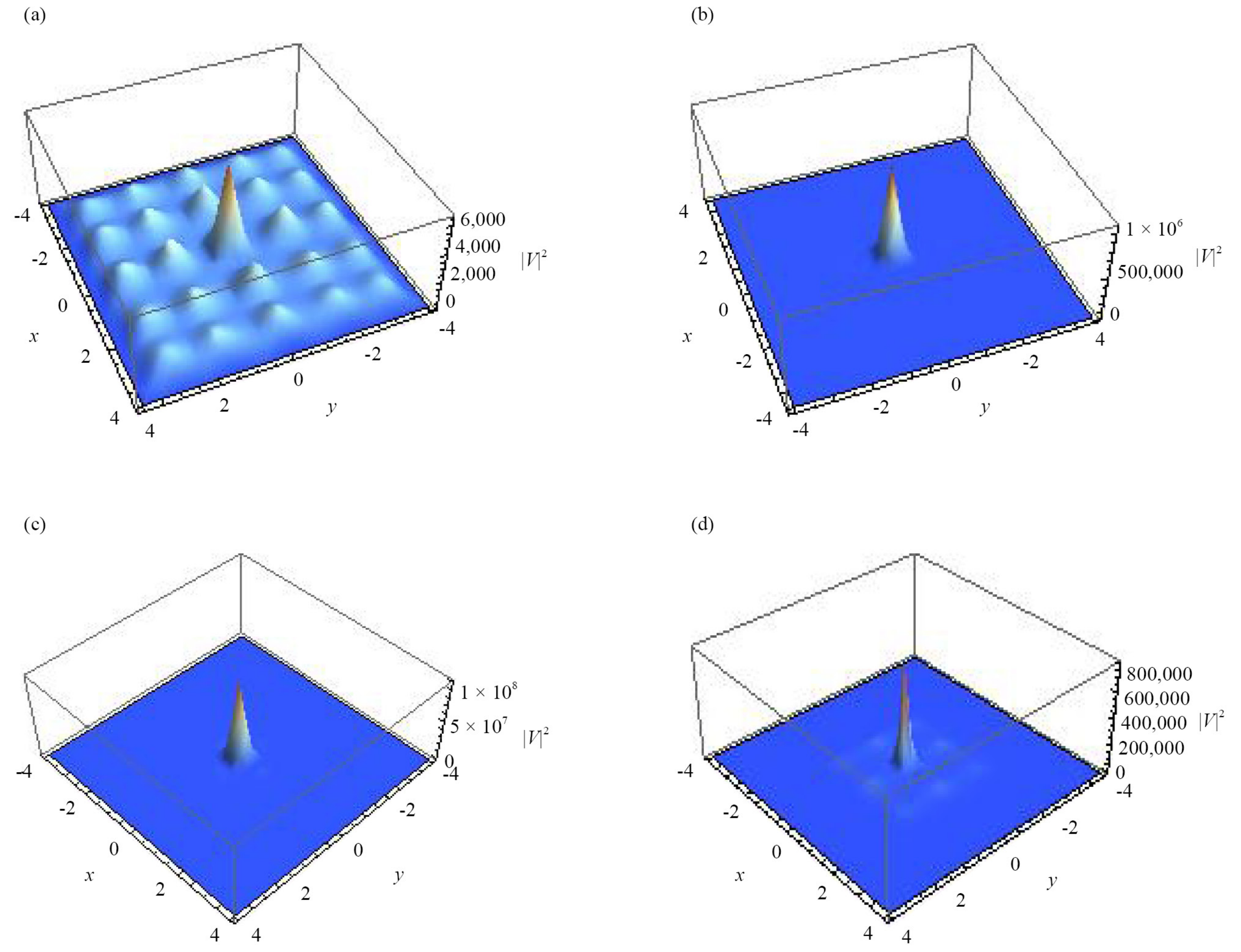

Figure 3. The formation of TFB as a result of spatial MI in MMs with cubic and quintic nonlinearities ($|\rho_1| = 1$ and $|\rho_2| = 0.1$), when cooperating ((a), (b) and (c)) and competing (d). Input perturbed continuous wave is the same as shown in Figure 2a. Other parameters are $P = 1$, $\Lambda = 0.001$ and $\eta = 4$

2.1 *Quantitative characterization of MI-induced localization*

To clarify the focusing characteristics of the generated structures, we quantify them using intensity-based metrics.

2.1.1 *Full Width at Half Maximum (FWHM)*

The transverse localization is characterized using the FWHM of the intensity profile $|V(x, y)|^2$. From numerical simulations (Figures 2-5), the typical width of the central filament is estimated as FWHM ≈ 0.6 to 1.0 (normalized units). This indicates strong spatial confinement compared to the computational domain $[-4, 4]$.

2.1.2 *Effective focusing distance*

We define an effective focusing distance z_f as the propagation distance at which the peak intensity is maximized: From the simulations, we obtain $z_f \approx 2.5$ to 3.6, with smaller values corresponding to enhanced MI gain in the presence of cooperating nonlinearities.

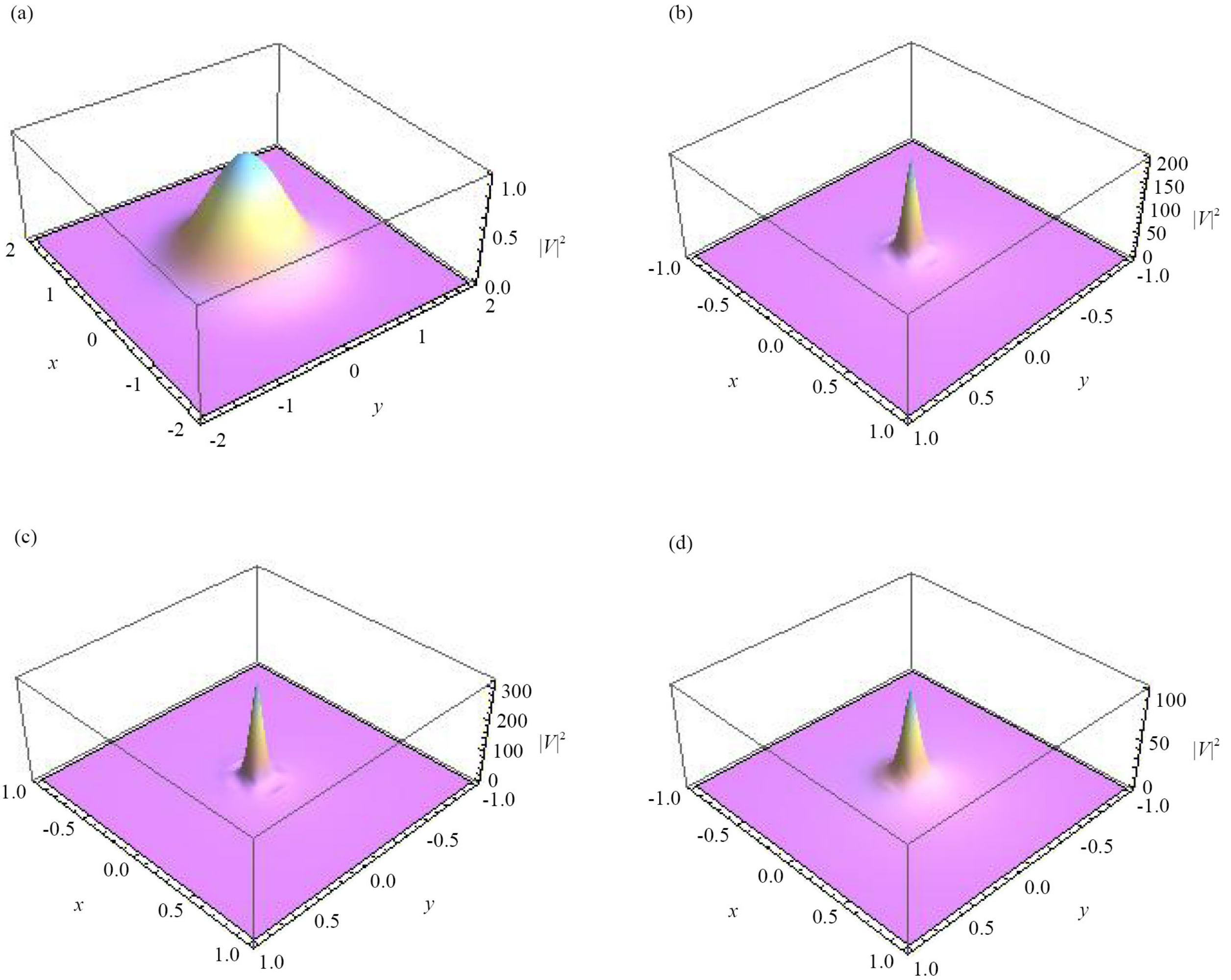

Figure 4. MI induced TFB formed during the evolution of a perturbed Gaussian beam with $P = 1$ in MMs. (a) Input intensity profile (b) cubic nonlinear case (c), MI enhanced cooperating cubic and quintic nonlinearities case, (d) MI suppressed competing cubic and quintic nonlinearities case. Other parameters are $|\rho_1| = 1$ and $|\rho_2| = 0.1$

2.1.3 *Effective numerical aperture*

Although no physical focusing system is present, an effective numerical aperture can be defined based on beam contraction:

$$\mathrm{NA}_{\mathrm{eff}} \sim \frac{w_0}{z_f}, \tag{17}$$

where w_0 is the transverse width (FWHM). Using the above estimates, we obtain

$$\mathrm{NA}_{\mathrm{eff}} \sim 0.15 \text{ to } 0.3. \tag{18}$$

This reflects moderately effective focusing induced purely by nonlinear self-action.

2.1.4 *Intensity gradient*

For potential optical trapping applications, the relevant quantity is the intensity gradient. A proxy for the gradient force is given by

$$F_{\text{grad}} \propto \nabla |V|^2. \tag{19}$$

The MI-induced filaments exhibit steep intensity gradients, indicating the possibility of strong transverse confinement forces.

3. Tailored TFB in MMs

Here, we numerically evolve a perturbed laser beam of two different intensity profiles (namely, Gaussian and hollow Gaussian) in nonlinear MMs with cubic and quintic nonlinearities. The particular emphasis will be given to address the generation of TFB with adjustable attributes using the tunable nonlinearities present in the MMs. Several studies have reported on the experimental realization of optical MMs with tunable nonlinearities. For example, the nonlinear responses exhibited by the fishnet MM [34], tunable third-order nonlinearity observed in Au/Al_2O_3 multi-layer MMs [35], the bulk nonlinear MMs for quantum application [36], and the adjustable nonlinearities observed in photonic MMs due to the combined action of resonances [37], to mention a few.

3.1 *MI induced TFB from Gaussian beam*

Now we numerically simulate the MI-induced TFB formed during the evolution of a perturbed Gaussian beam in MMs based on the model given in Eq. (1). We consider three nonlinear cases, namely (i) the Cubic case, (ii) the MI-enhanced cooperating cubic and quintic nonlinearities case, and (iii) the MI-suppressed competing cubic and quintic nonlinearities case. For the Gaussian intensity profile, the simulations are performed with the initial condition

$$V(0,x,y) = \sqrt{P}e^{-(x^2+y^2)}, \tag{20}$$

The corresponding intensity profile is depicted in Figure 4(a). When the laser beam with a Gaussian intensity profile numerically evolves through the MM, MI-induced TFB is formed, which is depicted in Figure 4. Figure 4(b) corresponds to the cubic nonlinearity case. Figure 4(c) corresponds to the MI-enhanced cooperating cubic and quintic nonlinearities case, where the laser beam is sharply focused with high peak intensity. Figure 4(d) corresponds to the MI-suppressed competing cubic and quintic nonlinearities case, where the peak intensity of the focused beam is much less than that of the cubic case.

3.2 *MI induced TFB from Hollow Gaussian Beam (HGB)*

To evolve HGB numerically, we consider a model for the initial intensity profile as

$$V(0,x,y) = \sqrt{P}(x^2+y^2)e^{-(x^2+y^2)}, \tag{21}$$

which is shown in Figure 5(a). Figure 5(b)-(d) present the numerically simulated evolution of optical filaments arising from a HGB. In contrast to the TFB generated from a conventional Gaussian input, the HGB profile inherently promotes the breakup of the beam into multiple localized filaments due to its annular intensity distribution. These filaments behave as strongly confined, high-intensity spots, leading to a more intricate and structured filamentation dynamics. As the propagation progresses, the HGB facilitates the formation of clustered TFB structures, where multiple filaments collectively organize along the initial ring profile. Notably, these TFB clusters preserve the annular geometry and exhibit a high degree of circular symmetry throughout their evolution. Furthermore, the MI-induced TFBs generated from the HGB configuration exhibit significantly higher peak intensities compared to those originating from a Gaussian beam. This enhancement can be attributed to the initial energy redistribution in the annular profile, which favors localized amplification at multiple azimuthal positions. Figure 5(b) illustrates the filamentation dynamics in the presence of purely cubic nonlinearity, where multiple well-defined filaments emerge along the ring, maintaining moderate peak intensities. In Figure 5(c), corresponding to the case of MI-enhanced cooperative cubic and quintic nonlinearities, the filaments become more sharply localized and exhibit substantially increased peak intensities, indicating stronger nonlinear focusing and energy confinement. In contrast, Figure 5(d) represents the regime of competing cubic and quintic nonlinearities, where MI is effectively suppressed. As a result, the resulting filaments are less pronounced, and their peak intensities are considerably reduced compared to the purely cubic case, reflecting the stabilizing influence of the competing nonlinear effects.

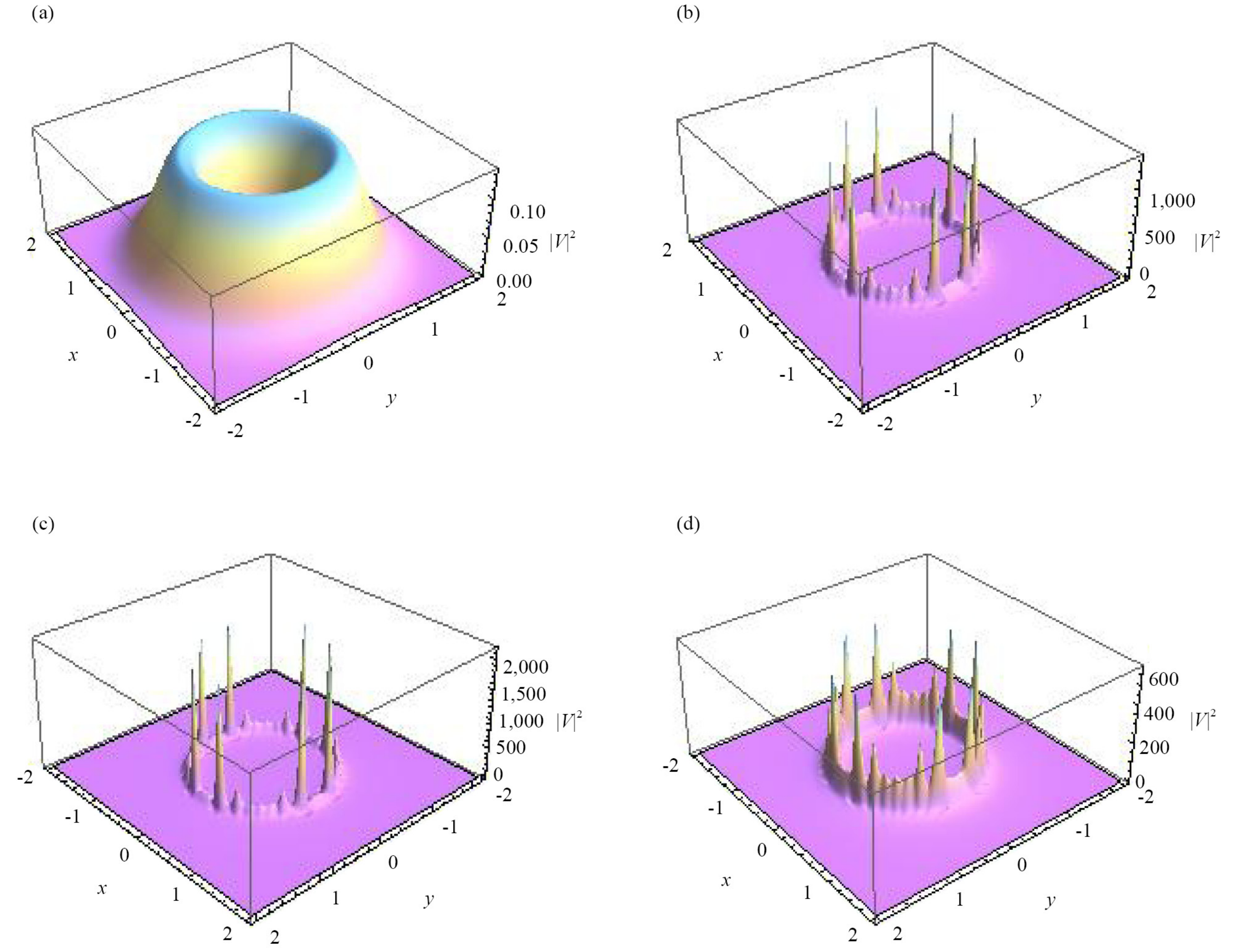

Figure 5. MI induced TFB formed during the evolution of a perturbed HGB with $P = 1$ in MMs. (a) Input intensity profile (b), cubic nonlinear case (c), MI-enhanced cooperating cubic and quintic nonlinearities case, and (d) the MI-suppressed competing cubic and quintic nonlinearities case. Other parameters are $|\rho_1| = 1$ and $|\rho_2| = 0.1$

4. Conclusion

In this study, we explored the impact of tunable optical nonlinearities on the generation of MI-induced tightly focused beams. Employing a linear stability analysis and numerical simulation on perturbed continuous waves, we identified the specific parameter regimes where continuous electromagnetic waves become unstable, thus facilitating the onset of modulation instability. Further, we have investigated the dynamics of Gaussian and hollow Gaussian intensity profiled laser beams with a particular emphasis on the generation of a tightly focused beam, adopting numerical analysis. Our result shows that the adjustable nonlinearities in the MMs provide large tunability to the attributes of the focused beam. Interestingly, HGB supports the formation of high-intensity TFB clusters as compared with a Gaussian intensity profile. The reported TFBs correspond to MI-induced self-focused filaments rather than externally focused diffraction-limited beams. The TFB has applications in optical trapping and high-density data storage.

Conflict of interest

The authors declare no competing financial interest.

References

[1] Kitamura K, Nishimoto M, Sakai K, Noda S. Needle-like focus generation by radially polarized halo beams emitted by photonic-crystal ring-cavity laser. *Applied Physics Letters*. 2012; 101: 221103.

[2] Dorn R, Quabis S, Leuchs G. Sharper focus for a radially polarized light beam. *Physical Review Letters*. 2003; 91: 233901.

[3] Li L, Zeng X, Gu M, Zhang Y, Sun R, Zhang Z, et al. Plasmonic metasurfaces for superposition of profile-tunable tightly focused vector beams and generation of the structured light. *Photonics*. 2023; 10(3): 317.

[4] Chen J, Wan C, Kong LJ, Zhan Q. Tightly focused optical field with controllable photonic spin orientation. *Optics Express*. 2017; 25(16): 19517-19528.

[5] Lin W, Huang H, Wen S, Xiao Y, Wu Z, Lian S, et al. Focusing properties and deep learning-based efficient tuning of symmetric butterfly beams. *Optics Letters*. 2025; 50: 2558-2561.

[6] Moradi H, Jabbarpour M, Abdollahpour D, Hajizadeh F. 3D optical trapping by a tightly focused circular airy beam. *Optics Letters*. 2022; 47: 4115-4118.

[7] Ramakrishna SA, Grzegorczyk TM. *Physics and Applications of Negative Refractive Index Materials*. 1st ed. CRC Press; 2008.

[8] Kivshar YS, Zhang X. Magnetic hyperbolic optical metamaterials. *Nature Communications*. 2016; 7: 11329.

[9] Lu M, Guo Z, Deng C, Hu X, Chen M. Tunable multiband asymmetric transmission based on flexible chiral metamaterial for refractive index sensing. *Journal of the Optical Society of America B*. 2025; 42: 419.

[10] Mousavi SA, Plum E, Shi J, Zheludev NI. Coherent control of optical polarization effects in metamaterials. *Scientific Reports*. 2015; 5: 8977.

[11] Solntsev AS, Agarwal GS, Kivshar YS. Metasurfaces for quantum photonics. *Nature Photonics*. 2021; 15: 327-336.

[12] Shaltout AM, Shalaev VM, Brongersma ML. Spatiotemporal light control with active metasurfaces. *Science*. 2019; 364(6441): eaat3100.

[13] Ren M, Cai W, Xu J. Tailorable dynamics in nonlinear optical metasurfaces. *Advanced Materials*. 2019; 32(3): 1806317.

[14] Lapine M, Shadrivov IV, Kivshar YS. Colloquium: nonlinear metamaterials. *Reviews of Modern Physics*. 2014; 86: 1093.

[15] Shao L, Zhu W. Recent advances in electromagnetic metamaterials and metasurfaces for polarization manipulation. *Journal of Physics D: Applied Physics*. 2024; 57: 343001.

[16] Keren-Zur S, Michaeli L, Suchowski H, Ellenbogen T. Shaping light with nonlinear metasurfaces. *Advances in Optics and Photonics*. 2018; 10: 309-353.

[17] Dudley JM, Genty G, Eggleton BJ. Harnessing and control of optical rogue waves in supercontinuum generation. *Optics Express*. 2008; 16: 3644.

[18] Daoui AK, Azzouzi F, Triki H, Biswas A, Zhou Q, Moshokoa SP, et al. Propagation of chirped gray optical dips in nonlinear metamaterials. *Optics Communications*. 2019; 430: 461-466.

[19] Triki H, Biswas A, Zhou Q, Mirzazadeh M, Mahmood MF, Moshokoa SP. Solitons in optical metamaterials having parabolic law nonlinearity with detuning effect and Raman scattering. *Optik*. 2018; 164: 606-609.

[20] Biswas A, Ekici M, Sonmezoglu A, Zhou Q, Alshomrani AS, Moshokoa SP. Solitons in optical metamaterials with anti-cubic nonlinearity. *The European Physical Journal Plus*. 2018; 133(5): 204.

[21] Shackeerali M, Ali AKS, Uthayakumar A. Impact of higher-order effects on modulation instability in negative index materials. *Optik*. 2022; 256: 168660.

[22] Wen S, Xiang Y, Dai X, Tang Z, Su W, Fan D. Theoretical models for ultrashort electromagnetic pulse propagation in nonlinear metamaterials. *Physical Review A*. 2007; 75: 033815.

[23] Zhang J, Wen S, Xiang Y, Wang Y, Luo H. Spatiotemporal electromagnetic soliton and spatial ring formation in nonlinear metamaterials. *Physical Review A*. 2010; 81: 23829.

[24] Ali AKS, Govindarajan A, Lakshmanan M. Stabilization of light bullets in nonlinear metamaterial waveguides. *Physical Review A*. 2022; 105(3): 033516.

[25] Scalora M, Syrchin MS, Akozbek N, Poliakov EY, Aguanno GD, Mattiucci N, et al. Generalized nonlinear Schrodinger equation for dispersive susceptibility and permeability: application to negative index materials. *Physical Review Letters*. 2005; 95: 013902.

[26] Essama BGO, Atangana J, Frederick BM, Mokhtari B, Eddeqaqi NC, Kofane TC. Rogue wave train generation in a metamaterial induced by cubic-quintic nonlinearities and second-order dispersion. *Physical Review E*. 2014; 90: 032911.

[27] Ali AKS, Govindarajan A, Lakshmanan M. Filamentation and stabilization of vortex solitons in nonlinear metamaterial waveguides. *Physics Letters A*. 2022; 451: 128416.

[28] Boardman AD, Grimalsky VV, Kivshar YS, Koshevaya SV, Lapine M, Litchinitser NM, et al. Active and tunable metamaterials. *Laser and Photonics Reviews*. 2011; 5(2): 287-307.

[29] Ghoshroy A, Özdemir SK, Güney DO. Loss compensation in metamaterials and plasmonics with virtual gain. *Optical Materials Express*. 2020; 10: 1862-1880.

[30] Agrawal GP. *Nonlinear Fiber Optics*. 3rd ed. San Diego: Academic Press; 2001.

[31] Shackeerali M, Ali AKS, Uthayakumar A. Tunable modulation instability spectra in negative index materials. *Results in Optics*. 2023; 13: 100520.

[32] Wen S, Wang Y, Su W, Xiang Y, Fu X, Fan D. Modulation instability in nonlinear negative-index material. *Physical Review E*. 2006; 73: 036617.

[33] Nath D, Roy B, Roychoudhury R. Periodic waves and their stability in competing cubic-quintic nonlinearity. *Optics Communications*. 2017; 393: 224.

[34] Tang S, Cho DJ, Xu H, Wu W, Shen YR, Zhou L. Nonlinear responses in optical metamaterials: theory and experiment. *Optics Express*. 2011; 19: 18283-18293.

[35] Genchi D, Balasa IG, Cesca T, Mattei G. Tunable third-order nonlinear optical response in ε-near-zero multilayer. *Physical Review Applied*. 2021; 16: 064020.

[36] Yesharim O, Hurvitz I, Foley-Comer J, Arie A. Bulk nonlinear metamaterials for generation of quantum light. *Applied Physics Reviews*. 2025; 12(1): 011323.

[37] Klein MW, Wegener M, Feth N, Linden S. Experiments on second- and third-harmonic generation from magnetic metamaterials. *Optics Express*. 2007; 15: 5238-5247.